Influence of the carrier wafer during GaN etching in Cl2 plasma

Thibaut Meyer, Camille Petit-Etienne, Erwine Pargon

Influence of the carrier wafer during GaN etching in Cl_2 plasma

Running title: Influence of the carrier wafer during GaN etching in Cl2 plasma

Running Authors: Meyer *et al.*

.

T. Meyer [1], C. Petit-Etienne [1] and E. Pargon [1,a)]

[1]Université Grenoble Alpes, CNRS, LTM, F-38000 Grenoble, France

[a)] Electronic mail: erwine.pargon@cea.fr

In this study we have performed a thorough characterization of GaN surface after etching up to 100 nm in Cl_2 plasma under various bias voltage and according to the carrier wafer used (Si, SiO_2, Si_3N_4, photoresist). The objective of this article is to evaluate the etch damage and contamination of the GaN surface when materials with other chemical nature are present during the etching. The effects of etching conditions on surface morphology and chemical compositions of etched GaN films are studied in detail using XPS and AFM measurements.

To this aim, an universal methodology is proposed to estimate accurately by XPS the stoichiometry of GaN surface exposed to reactive plasmas when only a Al Kα X-ray source is available. The results indicate that the GaN etching mechanisms are very sensitive to the chlorine radical density present in the plasma, the latter being strongly influenced by the carrier wafer. Substrates that are more chemically reactive with Cl_2 plasma such as silicon or photoresist compared to SiO_2 or Si_3N_4 will lead to a greater loading of atomic chlorine, which in turn will lead to lower GaN etch rates. Moreover, the GaN surface contamination will depend on the etch byproducts ejected by the carrier wafer.

The GaN surface exposed to Cl_2 plasma shows a Ga-depleted surface, because of the more important reactivity of Cl with Ga rather than N, except in the SiO_2 carrier wafer case. In this latter case, the formation of Ga-O bond limits the Ga removal. Regarding the surface roughness, it seems that the contaminants plays little role in the roughness formation except for the oxygen released by the SiO_2 carrier wafer.

On the other hand, the surface roughness evolution is clearly driven by chlorine radical flux reaching the GaN surface. At low bias voltage, a preferential crystalline orientation etching driven by the Cl radicals leads to the formation of hexagonal shaped defects that are associated to screw-type threading dislocations already present in the pristine GaN material. At higher bias, the enlargement of the defects is limited, leading to very low surface roughness value but to amorphized surfaces.

I. INTRODUCTION

Gallium nitride (GaN) semiconductor is now seriously considered as a choice material for high-power microelectronic devices because it can sustain high voltage and high current in extreme conditions. Moreover, GaN-based recessed gate architectures Metal-Insulator-Semiconductor High-Electron-Mobility-Transistor (MIS-HEMT) is a promising solution for the fabrication of normally-off transistor since it enables to keep high mobility and high density of electrons without compromising the voltage threshold[1]. However, some technological steps involved in the GaN-based MIS-HEMT fabrication are critical for the device performances. Among them, the plasma etching step dedicated to the gate recess patterning can lead to an electrical degradation of the GaN material because of the additional effects of UV photons, energetic ions and radicals during the

etching process[2-4]. In addition to these plasma-induced damages, the mismatch of lattice parameter and the thermal expansion coefficient between the GaN layer and the underlying material generate a high density of threading dislocations (10^7 to 10^{10} cm^{-2})[5], which are known to induce leakage paths in semiconductor devices[6-9].

The GaN gate recess process should provide a high etch selectivity to the mask material, an anisotropic profile and, above all, an undamaged surface. Chlorine-based precursors such as Cl_2 and BCl_3 have been widely used for the etching of GaN due to the volatility of $GaCl_3$, NCl_3 and N_2 species[10-12], whereas fluorine-based plasmas are known to form GaF_3 nonvolatile etch products. Several studies have already highlighted that halogen based plasma chemistries provide controlled etch profiles, low etch damages and smooth surfaces[13-16].

Similarly to silicon-based materials, GaN materials can be patterned directly with a photoresist mask printed by the lithography step or with an additional hard mask layer such as Si_3N_4 or SiO_2. The chemical nature of the mask used to transfer the pattern into the GaN plays a significant role in the process performance in terms of selectivity, pattern profile, surface roughness, etch rates, surface composition and contamination. Indeed, the wafer open area is usually about 50%, meaning that half of the material to be etched during the process is the mask. The interaction between the plasma species and the etched mask results in the production of undesired species in the plasma. Due to gas-phase reactions within the plasma such as recombination and ionization processes, the etch byproducts of the etching mask participate in the GaN etching mechanisms. In the same way, as GaN is an expensive material most GaN plasma process development requires to paste a small sample size (< 1*1 cm^2) on a carrier wafer. The chemical nature of the latter

can have impacts on the GaN etching mechanisms and the process performances. Zhirnov *et al.* reported different etch rates and surface roughnesses of GaN when changing the cathode materials (quartz, graphite), or when adding $SiCl_4$ to Cl_2 [17]. In the latter case, the authors observed a decreasing of the etch rates with the increasing $SiCl_4$ concentration. Ladroue *et al.* observed different morphologies according to the coverplate[18], and proposed a formation mechanism of columnar defects when using a SiO_2 coverplate. Urushido *et al.* studied the influences of Ge and Si on the GaN surface in a Cl_2 plasma, and highlighted the modification concerning the etch rates and etch profile[19]. To the best of our knowledge, the influences of the carrier wafer on the plasma composition and the GaN surface composition are not fully addressed. As undesired species are likely to generate interfacial traps in MIS-HEMT devices, it is mandatory to understand the etching mechanisms of GaN materials for a given mask or a given carrier wafer.

In this paper, we report on the physico-chemical modifications of a GaN surface exposed to a Cl_2 plasma as a function of both the carrier wafer (photoresist, SiO_2, Si_3N_4 and Si used), and the bias voltage that drives the plasma ion energy. Ellipsometry is used to estimate etched thickness and thus etch rates, X-ray Photoelectron Spectroscopy (XPS) analysis for the GaN surface composition and stoichiometry, and Atomic Force Microscopy (AFM) for the surface roughness. The objective is to evaluate the etch damage and contamination of the GaN surface when materials with other chemical nature are present during the etching. In addition to this, we propose a reliable and universal methodology to estimate accurately the GaN stoichiometry by XPS when only an Al Kα X-ray source is available on the XPS tool. It relies on the detailed peak decomposition of the N 1s / Ga $L_2M_{4,5}M_{4,5}$ region that allows extracting the contribution coming from the

N 1s only. This fitting procedure is universal and can be very useful to extract the N/Ga ratio by XPS when GaN is exposed to reactive plasmas.

II. EXPERIMENTAL

A. SET UP

Samples consisted of epitaxially grown 3.9 μm-thick GaN films on 4-inch sapphire (0001), commercialized by Lumilog. The experiments are performed in a 300 mm Centura® Advant- Edge™ MESA™ ICP (inductively coupled plasma) etch tool from Applied Materials. The plasma source consists of a dual RF coil operating at 13.56 MHz. The carrier wafer temperature and the reactor body are maintained at 60°C and 65°C, respectively. More details about the reactor can be found elsewhere[20]. In the present study, GaN samples are thermally glued with a thermal pasteat the center of a 300 mm carrier wafer. Several carrier wafers are used to investigate their impact on the GaN etch mechanisms: a bare Si wafer, or a Si Wafer on which either a 1 μm-thick photoresist is spin coated or a 100 nm-thick SiO_2 is thermally grown or a 55 nm-thick Si_3N_4 is deposited by Low Pressure Chemical Vapor Deposition. The GaN samples are exposed to Cl_2 plasma using the following conditions: the Cl_2 flow rate is 100 sccm, the pressure is 5 mTorr and the source power is 600 W. The bias power is the only parameter that is varied from 0 W to 90 W corresponding to a bias potential ranging from the plasma potential to − 200 V.

The GaN and carrier wafers etch rates are determined thanks to in situ ellipsometric measurements using an UVISEL ellipsometer from Jobin Yvon connected to the reactor. To measure GaN thickness before and after etching, spectroscopic acquisitions are performed between 2 and 3.2 eV with a step size of 0.005 eV. For all the experiments

except those with no bias power used, the etching times are adapted so that the GaN etched depths are similar of about 100 nm. An optical emission spectrometer (OES, Acton SP-500i) is used to identify the excited species during the etching process. The optical port is positioned at 5.4 cm above the carrier wafer. The slit size is fixed at 0.55 mm and the exposition time is set at 0.4 s. In order to reduce the noise, 50 spectra are recorded and averaged.

The surface roughness is measured using Atomic Force Microscopy (AFM, Dimension Icon bruker). The scan size is fixed at 5×5 μm^2 with 512*512 pixel resolution.

Surface composition and chemical environment are examined with quasi in situ Angle Resolved X-Ray Photoelectron Spectroscopy (ARXPS, Thermo Avantage Theta 300). The analysis chamber is directly connected to the reactor via a vacuum transfer chamber. X-ray photons are generated with a monochromatic Al Kα X-ray source (1486.6 eV). The pass energy and the energy step are set at 45 eV and 0.1 eV respectively. Low-energy electrons with Ar gas was used to compensate the surface charging. Due to the neutral gas introduction, the work pressure was 2×10^{-7} Torr in the analysis chamber. The angle-resolved capability of the Theta 300 is used for all analyses, with eight angles regularly spaced between 23.75° and 76.25° (*i.e.* collective angle), referred to the normal of the wafer.

B. XPS FITTING PROCEDURE

In the literature, there is no reliable methodology to extract properly the atomic chemical composition of a GaN surface by XPS, especially when GaN is exposed to reactive plasma species such Cl, F, Br that can form new chemical bonds with Ga such as Ga-Cl, Ga-F or Ga-Br. Indeed, if using an Al Kα XPS source, the Ga Auger $L_2M_{4,5}M_{4,5}$

lines overlaps with the N 1s core level, compromising the determination of the N content, while with a Mg Kα source (hυ = 1253.6 eV), the Ga $L_3M_{2,3}M_{4,5}$ Auger lines ($E_{kinetic}$ = 963-973 eV) and the Ga $L_3M_{4,5}M_{4,5}$ Auger lines ($E_{kinetic}$ = 1055-1070 eV) overlap with the C 1s and Cl 2p core levels, respectively, introducing uncertainties on the carbon and chlorine quantifications.

To obtain a complete GaN XPS analysis, it is optimal to use both Mg Kα and Al Kα sources in order to have information on the N 1s and the C 1s core levels. Unfortunately, not all XPS machines are equipped with both sources. In most published works using Al kα source only, the Ga $L_2M_{4,5}M_{4,5}$ Auger contribution is often represented with two or more peaks without constrained fit values, but more importantly, without physical meaning. The fit parameters of those Auger lines (peak position, Full Width at Half Maximum (FWHM), the Gaussian ratio) are determined for a reference sample and then the parameters are fixed and applied during the fitting procedure of the others samples[22]. This methodology may eventually work if all the analyzed samples present the same proportion of Ga chemical environment as the reference (Ga-N and Ga-O for instance), but fails if some new chemical Ga bonds are present. This is illustrated in Fig. 1 that shows the N 1s / Ga $L_{2,3}M_{4,5}M_{4,5}$ region obtained for a pristine GaN (with its native oxide) (Fig. 1a), and GaN films exposed to different reactive plasmas (Fig. 1b/c/d). It is obvious that the Ga $L_2M_{4,5}M_{4,5}$ Auger lines can be very different from a condition to another, and that the method consisting in fixing similar $L_2M_{4,5}M_{4,5}$ Auger lines parameters for all samples is not suitable. In the case of oxidized and fluorinated GaN surfaces (Fig. 1c/d), the N 1s signal (around 397.1 eV) is completely screened by the Ga $L_2M_{4,5}M_{4,5}$ signal, making difficult to extract the N 1s peak area with accuracy if no

method is applied. In this article, we propose an universal method of accurate, detailed peak decomposition of the N 1s / Ga LMM region when using only the Al Kα source for the XPS analysis. This procedure allows to accurately extract the contribution coming from the N 1s only, especially in the cases of GaN surface exposed to reactive plasmas.

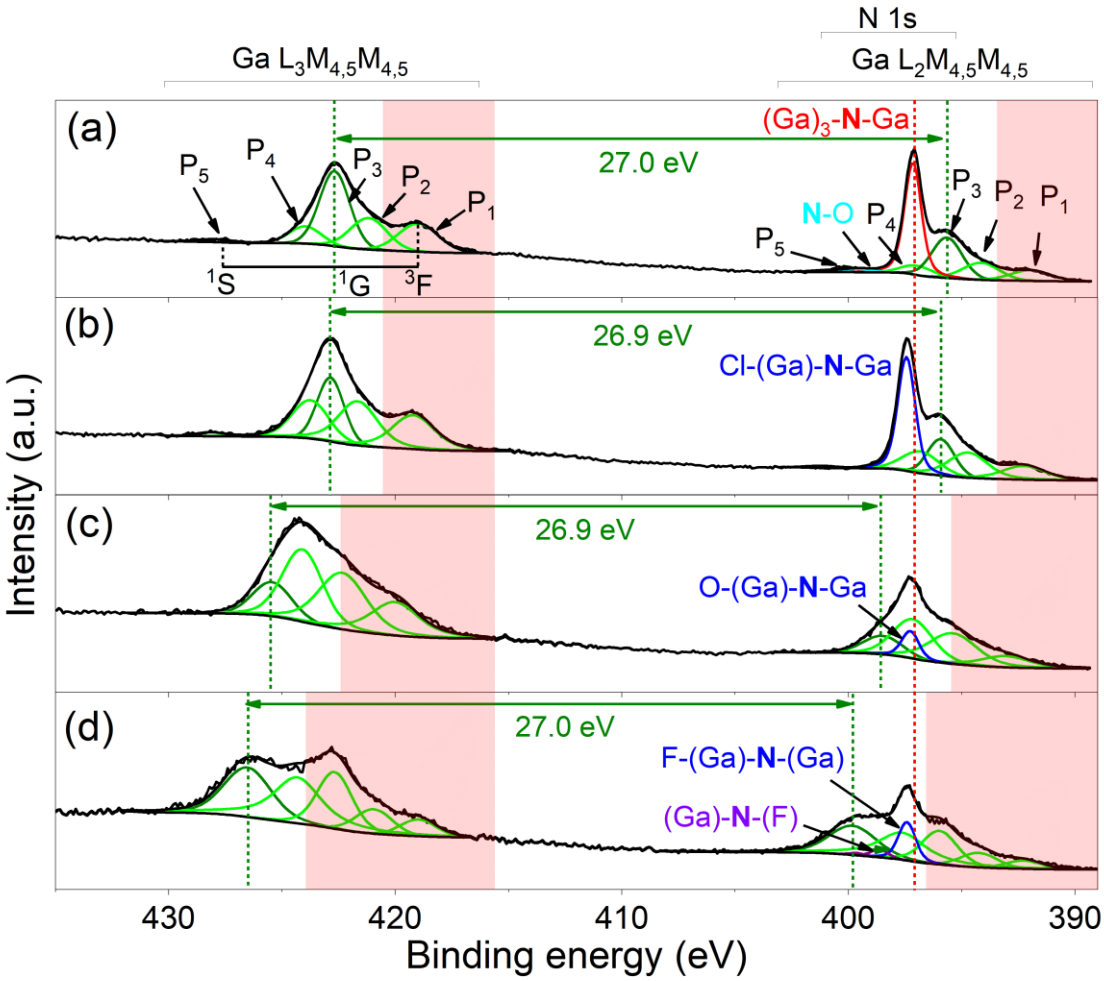

Fig. 1. N 1s XPS spectra at 76° recorded for (a) a pristine GaN sample and GaN exposed to (b) Cl_2 plasma (c) O_2 plasma (d) fluorocarbon-based plasma.

Before dealing with the fitting procedure, let's recall the Auger process leading to the Ga $L_{2,3}M_{4,5}M_{4,5}$ Auger lines. The latter transitions are initiated by the creation of L_2 and L_3 inner-shell holes, corresponding to the $2p_{1/2}$ and $2p_{3/2}$ core levels, respectively.

These core holes may be filled by $M_{4,5}$ outer shell electrons (*i.e.* Ga 3d core level), and a second electron may leave the $M_{4,5}$ shell with a kinetic energy depending on the binding energy of the three considered energy levels[23]. The kinetic energy difference between two identical final states (*e.g.* ^{1}G of Ga $L_2M_{4,5}M_{4,5}$ and ^{1}G of Ga L_3 $M_{4,5}M_{4,5}$), equals the spin-orbit splitting of the Ga 2p core level (ΔBE = 26.9 eV).

Besides the previously mentioned Auger transitions, the $L_2L_3M_{4,5}$ Coster-Kronig transition can occur and impact the shape of $L_2M_{4,5}M_{4,5}$ Auger lines[24-27]. For Ga-based materials, the Coster-Kronig transition does not occur because of the high Ga 3d binding energy ranging from 18 to 21 eV, and therefore, the Ga $L_2M_{4,5}M_{4,5}$ Auger lines have the same structure as the Ga $L_3M_{4,5}M_{4,5}$Auger lines. We emphasized that the absence of $L_2L_3M_{4,}$ Coster-Kronig transition is the condition sine qua none for the following fitting protocol.

Based on this, the proposed protocol requires to acquire both the Ga $L_2M_{4,5}M_{4,5}$ and Ga $L_3M_{4,5}M_{4,5}$ regions (Fig. 3a). The Ga $L_3M_{4,5}M_{4,5}$ is firstly decomposed in an arbitrary manner by using multiple peaks (noted P_x with x = 1,2,3,...), but the idea is to adjust perfectly the Ga $L_3M_{4,5}M_{4,5}$ envelop. The kinetic energy difference, the FWHM and the peak shape function are fixed and propagated on the Ga $L_2M_{4,5}M_{4,5}$ region (from 407 to 389 eV) without constraining the binding energy or the total area of the whole envelop (Table 1). In addition, the bulk plasmon of Ga $L_2M_{4,5}M_{4,5}$ and N 1s must be considered between 415 and 425 eV (red rectangle in Fig. 3), because it overlaps with the P_1 peak of the Ga $L_3M_{4,5}M_{4,5}$. That is why the peak area ratio is not constrained for the Ga $L_{2,3}M_{4,5}M_{4,5}$ Auger contributions at high kinetic energy (*i.e.* P_1 in Fig. 1a and Table 1). In case of oxygenated and fluorinated surfaces, the presence of additional ^{1}S and ^{1}G

final states, due to Ga-O and Ga-F chemical bonds, is likely to generate some uncertainties to the fitting procedure.

Ga $L_3M_{4,5}M_{4,5}$		*Ga $L_2M_{4,5}M_{4,5}$*		*ΔKE (eV)*	*FWHM (eV)*	*Peak area ratio*
Peak	KE (eV)	*Peak*	KE (eV)			
P_1	1067.7	P_1	1094.7		2.06	2.7
P_2	1065.5	P_2	1092.5		1.90	
P_3	1064.0	P_3	1091.0	27.0	1.57	1.6
P_4	1062.7	P_4	1089.7		1.64	
P_5	1058.7	P_5	1085.7		1.85	

Table 1: Parameters extracted from the fitting of Ga $L_{2,3}M_{4,5}M_{4,5}$ XPS spectrum of the pristine GaN (Fig. 1a). *KE: Kinetic Energy, ΔKE: Kinetic Energy difference between the P_x and $P_{x'}$ peaks (x = 1-5), FWHM: Full Width at Half Maximum; Peak area ratio: Area ratio between the P_x and $P_{x'}$ peaks (x = 1-5).*

The N 1s / Ga $L_2M_{4,5}M_{4,5}$ region is then adjusted using the predefined envelop for Ga $L_2M_{4,5}M_{4,5}$ and by adding peaks for the N 1s contribution. The Ga $L_{2,3}M_{4,5}M_{4,5}$ lines must be adjusted for each new samples given that the fitting parameters can be different from one sample to another. It should be noted that for all the data, the Ga $L_2M_{4,5}M_{4,5}$ Auger peak positions itself at -26.95 ± 0.1 eV from the Ga $L_3M_{4,5}M_{4,5}$ during the fitting procedure, which is the separation between the Ga $2p_{3/2}$ and Ga $2p_{1/2}$ core level ($\Delta E = -26.9 \pm 0.1$ eV), confirming the relevance of the protocol. The main advantage is that the fitting procedure provides a physical meaning to the resulting Ga $L_2M_{4,5}M_{4,5}$ decomposition because it is entirely based on the Ga $L_3M_{4,5}M_{4,5}$ feature. The N 1s core

level of the pristine material shows a major contribution at 397.1 eV, with a FWHM constrained between 0.8 and 0.9 eV, corresponding to $(Ga)_3$-N-Ga bonds and a small contribution only visible at grazing angle at 399.8 eV corresponding to N-O bonds (see Fig. 1a).

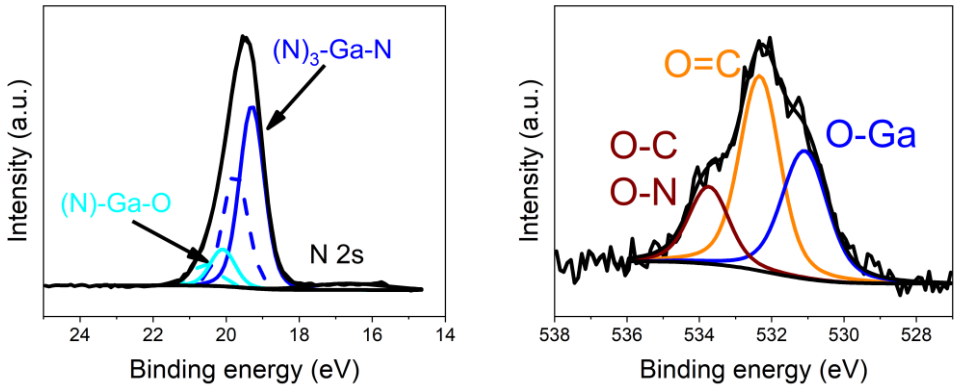

Fig. 2. (a) Ga 3d (b) O 1s XPS spectra at 76° of a pristine GaN sample.

Regarding the fitting procedure for the Ga 3d peak, most publications use one peak that encompasses the Ga $3d_{5/2}$ and Ga $3d_{3/2}$ doublet, generally positioned between 19.3 to 20.3 eV for Ga-N bond[28-32]. In this work, each Ga 3d component is fitted with a doublet using a spin-orbit splitting of 0.45 eV and an area ratio between the $d_{5/2}$ and $d_{3/2}$ components of 0.66[33-36]. The XPS spectra of the pristine GaN is calibrated in energy by fixing the C-C peak position of the carbon contamination at 284.8 eV. Figure 2a shows the decomposition of the Ga 3d peak for a pristine GaN with its native oxide. It is fitted with two doublets with Ga $3d_{5/2}$ components located at 19.3 eV and 20.1 eV and corresponding to $(N)_3$-Ga-N and (N)-Ga-(O) bonds respectively. The shift of + 0.85 eV for the oxidized Ga component is consistent with literature[37]. After GaN etching in Cl_2

plasma, there is no more carbon. The spectra are thus calibrated in energy by using the $(N)_3$-Ga-N (Ga $3d_{5/2}$) environment located at 19.3 eV.

Turning to the O 1s core level (Fig. 2b), it can be decomposed into three components. The peak at 531.0 eV is assigned to the (N)-Ga-O chemical state[38]. The peaks at 532.3 and 533.7 eV are attributed to O=C and O-C chemical states, respectively. It is expected that the O-N chemical state overlaps with the O-C and O=C contributions.

Due to the angle-resolved capability of the ARXPS, it is possible to investigate different probed depths as a function of the collection angle. The considered probed depth equals to 3 times the inelastic mean free path, for a given photoelectron kinetic energy, and corresponds to 95% of the collected signal. Based on the NIST calculation[39], the probed depths are calculated for N 1s, Cl 2p, Ga 3d core levels and plotted in Fig. 3. This work is focused on the surface angle (76°) because it permits to study the reactive layer composition located on the near surface (< 1.8 nm), whereas for the bulk angle (23°), the reactive layer contributions (Cl 2p, C 1s, Si 2s) are screened by the bulk signal. The N/Ga ratio for the pristine material is estimated by taking into account all Ga (Ga-N + Ga-O) and N (N-Ga and N-O) contribution. For an XPS angle analysis of 23.6° that mainly probes the GaN bulk, this ratio is found to be 1.06. This value will be used as our reference ratio for the GaN stoichiometry.

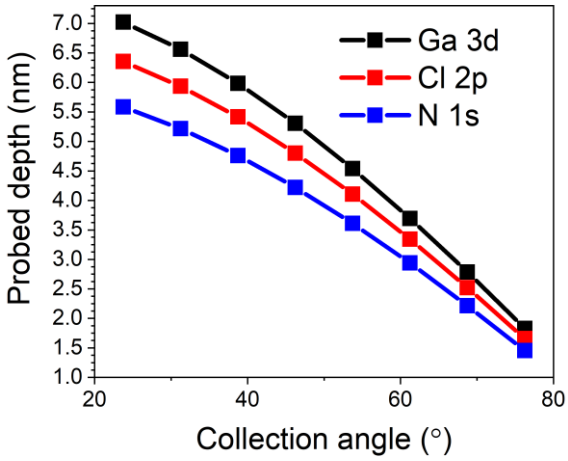

Fig. 3. Ga 3d, Cl 2p and N 1s probed depths as a function of the collection angle.

III. RESULTS AND DISCUSSION

A. GaN and carrier wafers etch rate in Cl_2 plasma

Figure 4 shows the vapor pressure data of the stable neutral species expected during the Cl_2 etching of GaN ($GaCl_3$, NCl_3) as well as Si, photoresist, SiO_2 and Si_3N_4 carrier wafers. It is known that $SiCl_4$ is the main etch byproducts during the etching of Si in a Cl_2 plasma. The etching of photoresist carrier wafers is likely to form the volatile CH_xCl_y reactive neutral species. In addition, the presence of hydrocarbon species may form hydrocarbon etch products such as $Ga(CH_3)_3$. For the SiO_2 and Si_3N_4 carrier wafer, gas-phase reactions are likely to form SiO_x or SiN_x reactive neutral species which are nonvolatile. In the latter case, there is no data available because Si_3N_4 is one of most thermodynamically stable material.

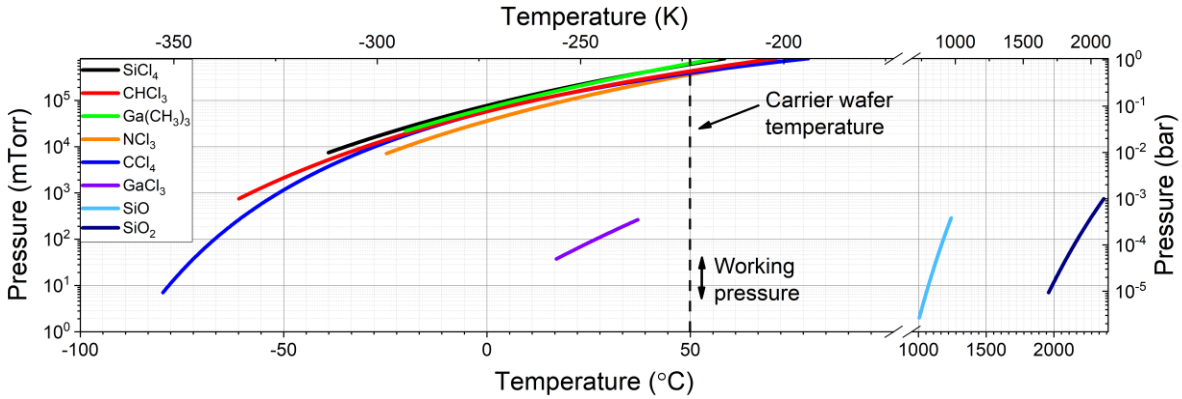

Fig. 4. Vapor pressure data calculated from[40-44].

Vapor pressure data gives only a simple interpretation of the chemical etching mechanism, and the respective volatility of the etch byproducts of the different materials used in this study.

GaN samples are patched on four different carrier wafers and exposed to a Cl_2 plasma using the conditions mentioned in the experimental set up. Only the bias power has been varied from 0 W to 90 W corresponding to a bias potential of V_p to − 200 V. Fig. 5a shows the carrier wafer etch rate, the GaN etch rate and the selectivity as a function of bias potential and according to the chemical nature of the carrier wafer. Due to the physical properties of each wafer, the plasma/surface interactions are necessarily different even during the exposition to a near-identical Cl_2 plasma.

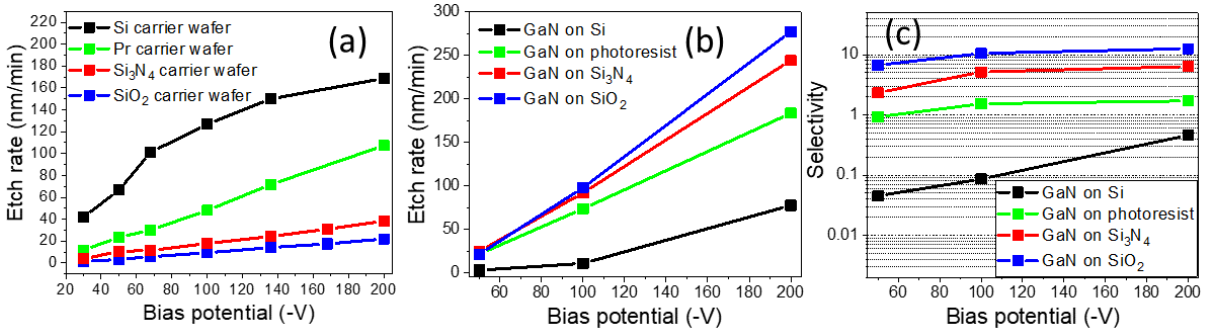

Fig. 5. (a) Carrier wafer etch rate (b) GaN etch rate (c) selectivity as function of the bias potential used for the Cl2 etching process.

The Si carrier wafer is clearly etched faster, followed by the photoresist, $S_{i3}N_4$ and SiO_2 carrier wafers. This is not surprising considering the bond dissociation energy of the involved bonds which are 310 ± 1.2 kJ/mol for Si-Si, 338.4 ± 1.2 kJ/mol for C-H, 437.1 ± 9.9 kJ/mol for Si-N and 799.6 ± 13.4 kJ/mol for Si-O[45]. The volatility of the would-be etch byproducts is also a critical parameter, with $SiCl_4$ and CCl_4 the most volatile etch products (Fig. 4). Overall, the etch rate logically increases with ion energy because of the increasing sputtering yields. For low-bias processes ($|V_p| \leq |V_{DC}| \leq 50$ V), the etch rates are similar for the photoresist, Si_3N_4 and SiO_2 carrier wafers. In such cases, the physical part of the etching is considerably reduced, and the etching relies mostly on the chlorine adsorption and etch byproducts desorption.

Figure 5b shows the impact of the carrier wafer on the GaN etch rate. In the present case, there is a relation between the carrier wafer etch rates and the GaN etch rates because of the chlorine consumption by the wafer. The more rapidly the carrier wafer is etched, the lower the GaN etch rate is. This is due to loading effect, the chemical reactive neutrals (and mainly the atomic chlorine) are consumed by the carrier wafer and are less available for the GaN etching. The GaN etch rate also increases with ion energy. Similar results were obtained by Chang et al. with Ni, SiO_2 and photoresist masks[46].

Regarding the etch selectivity (Fig. 5c), selectivity above 1 can be easily achieved with SiO_2 and Si_3N_4, while for the photoresist and Si carrier wafers, the chlorine consumption caused the major difference in term of selectivity. The best selectivity is found with the SiO_2 carrier wafer and the lowest selectivity when using a Si carrier wafer.

In literature, it has been observed a higher selectivity for GaN:SiO_2 (mask) than for GaN:photoresist (mask)[46-48].

B. *Optical Emission analyses during Cl_2 etching*

Fig. 6 shows optical emission spectra recorded during the etching of Si, photoresist, Si_3N_4 and SiO_2 carrier wafers with a bias power of 90 W (V_{DC} = − 200 V). A Cl_2 reference spectrum, obtained without carrier wafer, is presented in Fig. 6a for comparison purposes. The emission spectrum during the etching of Si carrier wafer in a pure Cl_2 plasma is plotted in Fig. 6b, in which Cl_2 vibrational bands, Cl emission lines and Si emission lines are observed in the UV region. Furthermore, the distinct features of SiCl, $SiCl_2$ and $SiCl_3$ vibrational bands are detected around 280, 330 nm and 390 nm, respectively[49]. This confirms the production of SiCl etch byproducts during the Si etching in Cl_2 plasma.

Presence of Si excited lines and SiCl vibrational band are also observed during the etching of the Si_3N_4 carrier wafer (Fig. 6e). In addition, the ejection of nitrogen is indirectly evidenced with the formation of N_2 vibrational bands (from 300 to 400 nm), resulting of gas-phase recombination and subsequent excitation by electron impact. Turning to the SiO_2 carrier wafer (Fig. 6d), there are weak Si emission lines and a weak SiCl emission band. However, despite the etching of SiO_2 (See. Fig. 5), the oxygen triplet at 777 nm remains undetected regardless of the bias potential. It is though that the oxygen, which is released from the carrier wafer, reacts to form SiO or SiOCl species within the plasma. Nevertheless, the SiO vibrational bands range from 216 to 293 nm[50], and thus overlap with the Cl2 vibrational band.

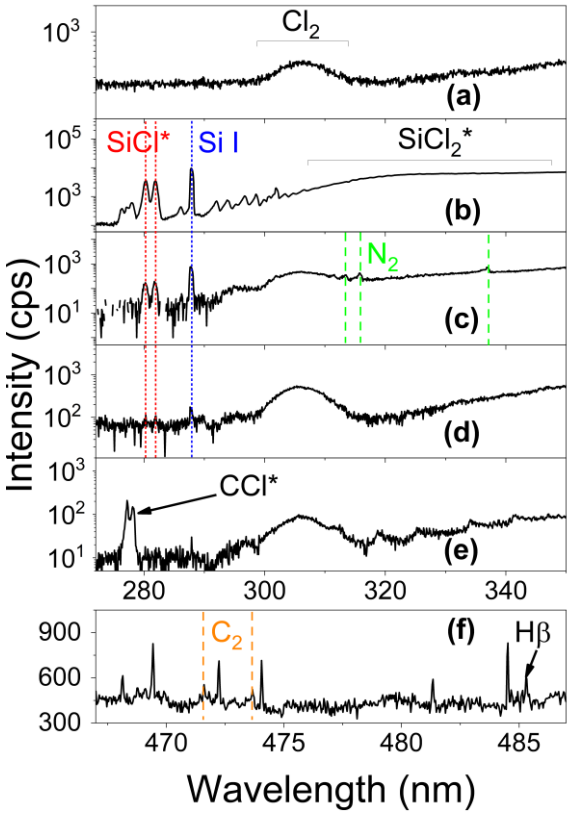

Fig. 6. Optical emission spectra recorded during Cl_2 etching (a) without wafer (b) with Si (c) with SiO_2 (d) with Si_3N_4 and (e) with photoresist carrier wafers at − 200 V in the UV region; (f) Optical emission spectrum recorded during Cl_2 etching of photoresist carrier wafer at − 200 V in the visible.

It should be pointed out that $SiCl_2$ and $SiCl_3$ vibrational bands cannot be clearly detected during the etching of the SiO_2 and Si_3N_4 carrier wafers.

Given that the photoresist wafer (Fig. 6c) is mostly composed of hydrocarbon species, C and H atoms eventually reacts with Cl atoms at the surface or in the volume. Fig 6e indeed confirms the formation of CCl etch by products, while Fig. 6f highlights the presence of C_2 vibrational bands (Swan bands) and H balmer series

.

The reaction path for the formation of C_2 excited species is not clear given that such species could be a result of CCl_x or/and CH_x recombination processes and subsequent excitation processes. the negligible intensity of Hβ could be caused by the recombination processes between H and Cl/Cl_2 species to produce HCl, but the latter species cannot be detected in the visible spectral range. Optical emission spectroscopy provides a simple analysis of plasma chemistry. It can be extrapolated that the presence of excited species (C_2*, $SiCl_x$*, N_2*, H balmer series) conveys the presence in the plasma of positives ions (CCl_x^+, $SiCl_x^+$, N_x^+, H_x^+) and reactive neutral species ($SiCl_x$, CCl_x, N, C_xH_y) that will interact with the GaN substrate during the etching process. The amount of contaminants detected by OES is well correlated with the carrier wafer etch rate of Fig 5a, namely that the OES spectra of Si and PR substrates that are etched faster show more intense new emission lines.

C. GaN surface composition after etching in Cl_2 plasma

As it will be detailled later in this article, after GaN etching in Cl_2 plasma, Cl is detected on the GaN surface whatever the nature of the carrier wafer. In the case of Si carrier wafer, Si is also detected while in the case of photoresist, C is detected. The other contaminants that can be detected in a few amount are O and F that come from the reactor wall. In the case of the SiO_2 carrier wafer, O can also come from the carrier wafer.

We will first focus on the XPS spectra deconvolution of N 1s, Cl 2p, Ga 3s, Si 2s and Ga 3d core levels recorded at a collection angle of 76° (surface angle) after the

etching of GaN with different carrier wafers at − 100 V in a Cl_2 plasma (Fig.7). Table 2 lists the binding energy extracted from the XPS spectra deconvolution.

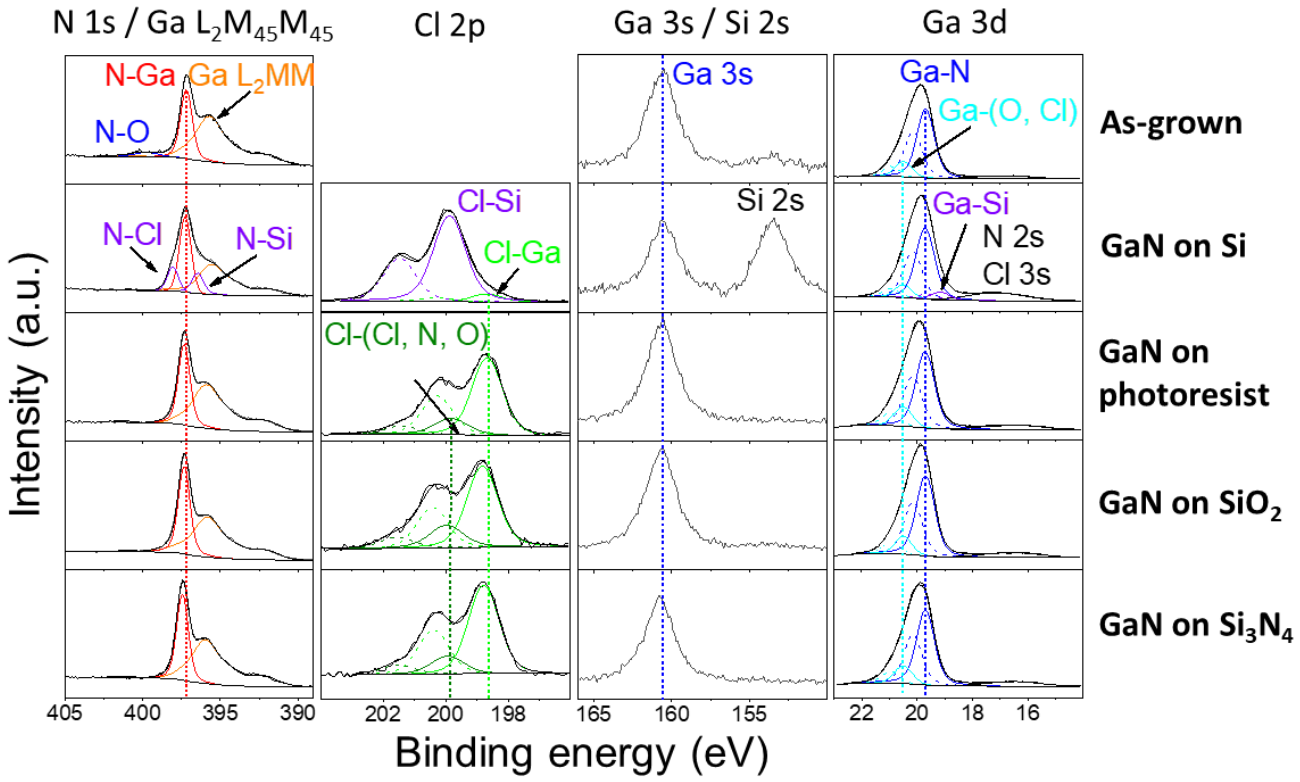

Fig. 7. N 1s, Cl 2p, Ga 3s, Si 2s and Ga 3d XPS spectra (collection angle = 76°) recorded after GaN etching in Cl_2 plasma at − 100 V bias voltage according to the carrier wafer used.

Element	*Core level*	*Environment*	*GaN on Si*	*GaN on photoresist*	GaN on SiO_2	*GaN on Si_3N_4*
N	1s	Cl-(Ga)-**N**-(Ga)	397.3	397.3	397.3	397.4
		(Ga)-**N**-Cl	397.9			
		(Ga)-**N**-Si	396.5			
Ga	$3d_{5/2}$	(N)-**Ga**-Si	18.7			
		(N)-**Ga**-N	19.3			
		(N)-**Ga**-Cl	20.1			
Cl	$2p_{3/2}$	**Cl**-Ga	198.1	198.1	198.4	198.4
		Cl-(Cl, Si, N)	199.3	199.3	199.6	199.6
Si	2s	**Si**-(N, Cl)	153.1			
C	1s	**C**-Ga		284.0		

Table 2: Binding energy values (± 0.2 eV) of N 1s, Ga 3d, Cl 2p, Si 2s and C 1s peaks after GaN etching in Cl_2 plasma at − 100 V bias voltage according to the carrier wafer used.

The deconvolution of Ga 3d, N 1s and Cl 2p peaks are similar for photoresist, SiO_2 and Si_3N_4 carrier wafer. The case of Si wafer showing different chemical environments is discussed afterwards.

The Ga 3d is deconvoluted with two doublets with the Ga $3d_{5/2}$ peaks located at 19.3 eV and 20.1 eV. The first doublet is assigned to the (N)-Ga-N chemical states, while the second doublet with a higher chemical shift of + 0.8 eV is attributed to Ga-Cl or Ga-O chemical bond. No $GaCl_2$ or $GaCl_3$ bonds are detected since these chemical environments present higher chemical shift of + 1.3 eV[51] and + 2.3 eV[34], respectively.

The Cl 2p spectra are fitted with two doublets, with a spin orbit separation of 1.6 eV and 2:1 peak area ratio, and shows two chemical environments. The major one corresponds to Ga-Cl bonds at 198.2 ± 0.2 eV. The other one is located at 199.4 ± 0.2 eV and could be mainly attributed to physisorbed Cl_2[51].

In the case of photoresist substrate, C is also detected on the GaN surface. The main peak is located at 284.0 eV that we attribute to C-Ga chemical bonds. Some very weak contributions can be found at 286 eV and 289 eV and can be attributed to CCl and CCl_2 bonds but the signals of those bonds constitutes less than 2% of the total atomic concentration.

The N 1s core level shows only one contribution positioned at 397.3 ± 0.1 eV. However, it should be noticed that the N 1s peak position is slightly shifted of + 0.2 eV compared to the pristine material. We attribute this slight shift to higher energy as a second neighbouring effect due to the presence of Cl-(Ga)-N-Ga bonds rather than solely (Ga)-N-Ga.

Regarding the Si substrate, in addition to the peaks mentioned above for the other substrates, $SiCl_x$ species are also detected as revealed by the Cl $2p_{3/2}$ peak at 199.5 eV and the Si 2s peak at 153.1 eV (+ 2.5 eV chemical shift that can only be attributed to $SiCl_2$/$SiCl_3$ species)[52]. The N 1s peak presents also two new contributions at 396.5 eV and 397.9 eV that we attribute to (Ga)-N-Si and (Ga)-N-Cl bonds. Furthermore, the Ga 3d core level is slightly affected by the presence of Si/$SiCl_x$ at the surface. Another contribution must be added at 18.7 eV and it is associated to the Ga-Si chemical state.

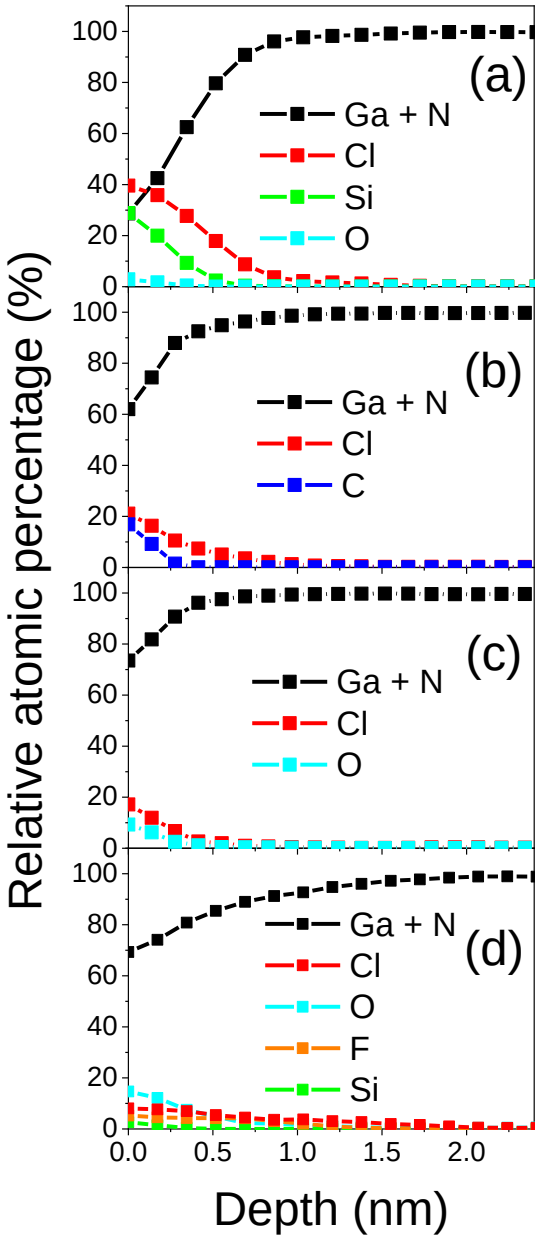

Fig. 8. In-depth profiles of atomic elements present on GaN surface after etching in Cl_2 plasma at − 100 V bias voltage with (a) Si (b) photoresist (c) Si_3N_4 (d) SiO_2 carrier wafer. The profiles are obtained from the ARXPS data.

Thanks to the angle resolved capability of our XPS, the in-depth profile of the contaminant concentrations on the GaN surface exposed to Cl_2 plasma at − 100 V can be plotted (Fig 8).

Regarding the Si carrier wafer (Fig. 8a), a mixed $SiCl_x/GaCl_x$ layer is present on the first 0.5 nm and Cl penetrates slightly deeper in the GaN up to 0.8 nm. Turning to the photoresist carrier wafer in Fig. 8b, it appears that the first 0.5 nm is composed of GaN reactive layer rich in C and Cl. This mixed layer is certainly composed of the Ga-N, C-C, C-Cl and Ga-Cl bonds that we have identified on the XPS spectra. The chlorine penetrates deeper up to 0.8-1 nm as in the Si case. We cannot exclude that the hydrogen present in the photoresist and released in the plasma during the etching (as evidenced by the OES) interacts with the GaN surface and creates some deeper damage but it cannot be highlighted by XPS. With the Si_3N_4 carrier wafer (Fig. 8c), a very thin GaOCl reactive layer is formed on the very first 0.5 nm. The surface seems to be less deeply modified than in the two previous cases. Finally, with the SiO_2 carrier wafer (Fig. 8d), the Si is detected in a very few amount compared to oxygen and is located at the extreme surface (0.5 nm). This may suggest that the oxygen that is detected deeper is linked to Ga and compete with chlorine to form either Ga-O or Ga-Cl bond. Unfortunately, it is impossible to distinguish Ga-Cl or Ga-O bonds on the Ga3d core level, since they present similar chemical shifts. Finally, the ARXPS data indicates that the GaN surface is more deeply impact up to 1 nm. However, as evidenced by the AFM measurements of next section, the surface roughness is very high for the SiO_2 carrier wafer at – 100 V, so it is hard to clearly conclude on the species penetration in this case compared to the other substrates.

From this first analysis of the XPS data, it appears that the Si_3N_4 substrate seems to be the one providing the thinnest reactive layer, and the shallowest chlorine penetration compared to Si and PR carrier wafers.

Molecular dynamics simulations, dealing with the surface modifications of Si exposed to chlorine plasmas[53], show that there are two main parameters that drive the thickness of the SiClx reactive layer that forms on the Si surface during the etching: the ion energy and the neutral over ion flux ratio (Γ_n/Γ_i). Higher ion energy or lower Γ_n/Γ_i leads to thicker reactive layer. They also observed that the thicker the reactive layer the lower the etch rate.

For all the carrier wafers, the ion energy used is similar of 100 eV but the chemical nature of the ion is different. From the OES data, it is suspected that heavy $SiCl_x^+$ dominates over Cl^+/Cl_2^+ in the case of Si, while Cl^+/Cl_2^+ ions may be the majority ions for the two Si_3N_4 and SiO_2 carrier wafers. According to the molecular ion implantation Theory[54], the net ion energy is given by Em/M, where E is the energy of the molecular ion, m is the mass of the atom, and M is the total mass of the molecule. Therefore, with polyatomic ions, the net energy of the energetic atoms reaching the surface is much less than the energy of the atoms issued from monoatomic ions reaching the surface. For example, the net energy of chlorine atoms reaching the surface as a $SiCl_2^+$ molecular ion with a given energy is 36% less than the energy of a Cl^+ atomic ion reaching the surface with the same given energy. Consequently, the penetration depth of chlorine ion should be less in the case of PR and Si substrates than in the Si3N4 case, which is not what we observe. In contrast, for Si and PR substrates, it is likely that the atomic chlorine concentration in the plasma is greatly reduced due to the carrier wafer

consumption, which may lead to a decrease of Γ_n/Γ_i, which in turn would lead to a thicker reactive layer as predicted by Paulin et al.

Besides, for an equivalent energy, heavy molecular ions ($SiCl_x^+$, CCl_x^+) may less penetrate in the GaN surface explaining why Si and C species are mainly located at the very near surface.

Our data indicates that the reactive layer thickness, and thus the GaN etch rate, is mainly driven by the atomic chlorine radical present in the plasma. This explains why the reactive layer is thinner in the Si_3N_4 carrier wafer case and why higher etch rates are obtained.

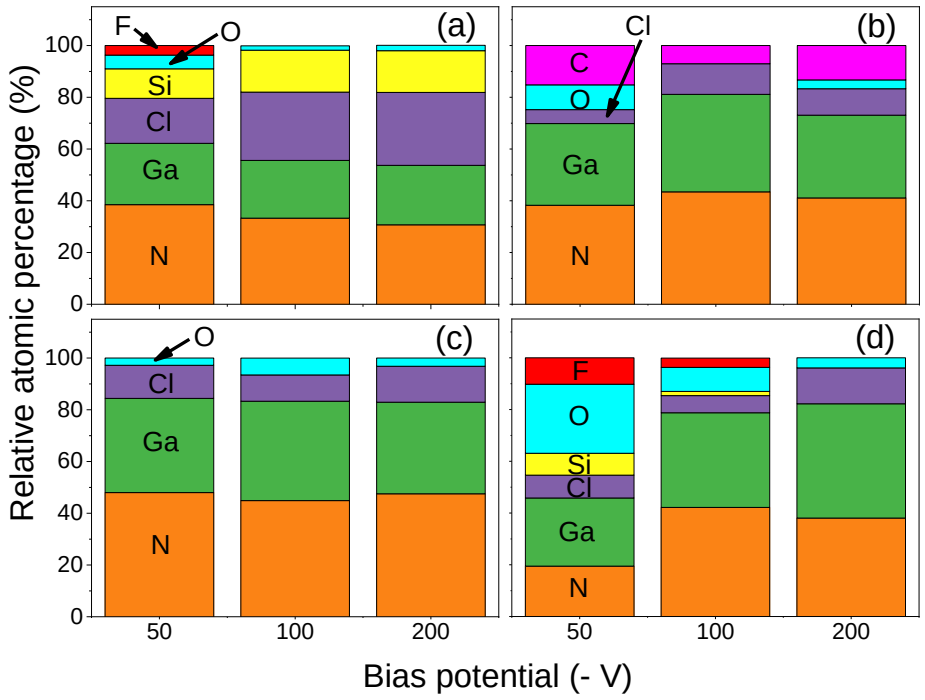

Fig. 9. XPS surface composition (collection angle = 76°) of GaN surface after etching in Cl_2 plasma according to the bias potential voltage with (a) Si (b) photoresist (c) Si_3N_4 (d) SiO_2 carrier wafer.

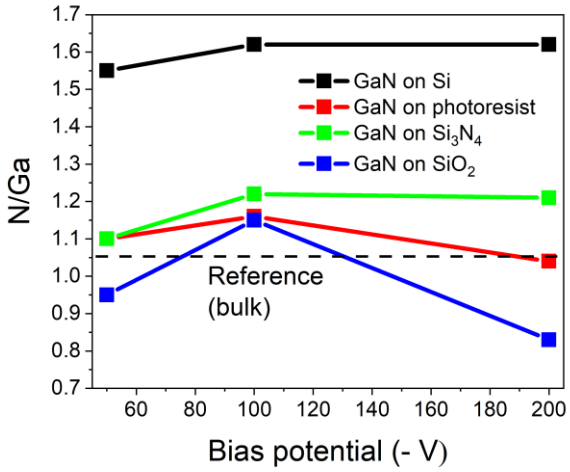

Fig. 10. N/Ga ratio according to the bias potential and the carrier wafer.

Surface chemical compositions extracted from the deconvolution of the XPS peaks obtained at a collection angle of 76° according to the carrier wafer and the bias potential are shown in Fig. 9. Similar XPS spectra deconvolution as described previously has been used and no other chemical environments were identified with other bias voltages.

Regarding the Si wafer (Fig. 9), $SiCl_x$ species are detected for all bias potential and their contribution to the chemical composition of the probed surface increases from 14.1% to 26.1% when increasing the bias voltage. As mentioned earlier, the $SiCl_x$ species come from the etching of the Si substrate, and their concentration in the plasma phase increases with increasing bias power, since the Si etch rate increases (see Fig. 4). These etch byproducts are likely to be ionized and then participate to the etching of the GaN material.

In the case of a photoresist substrate (Fig. 9b), the carbon contamination constitutes between 8% and 15% of the total chemical quantification at the surface, showing no clear trend with increased bias voltage. Some O contamination is also randomly detected.

For Si_3N_4 carrier wafer, the reactive layer on the GaN surface is similar for all bias substrate. It remains very thin and is mostly composed of (N)-Ga-Cl species with some O contamination coming from the reactor wall.

Finally, for the SiO_2 substrate, SiO_x contamination can be detected for all bias voltage (Fig. 9d). At − 50 V, we could clearly identify two O 1s contributions at 531.0 eV and 532.6 eV, assigned to O-Ga and O-Si chemical states. It is observed that the SiO contamination on the GaN surface decreases with the bias voltage increase. This could be in contradiction with the highest SiO_2 etch rate at higher bias, releasing even more oxygen and silicon in the plasma. However, the higher bias voltage may facilitate the sputtering of SiO_x products that deposit on the GaN surface.

To go deeper in the analysis the N/Ga ratio is plotted in Fig. 10 as a function of the bias voltage and the substrate used and compared to the reference N/Ga ratio of 1.06.

Except for the SiO_2 carrier wafer, there is a Ga depletion at the GaN surface that is slightly enhanced by the bias voltage, but the trend is not so clear. This Ga depletion is especially pronounced in the case of the Si carrier wafer. Other studies dealing with GaN etching in Cl_2 plasma have shown that Cl preferentially reacts with Ga rather than N to form volatile $GaCl_x$ products. Hasegawa *et al.* highlighted a N-enrichment, in a Cl_2/Ar ALE process, attributed to $GaCl_3$ volatily after a chlorination step[51]. Kim *et al.* observed a N-rich surface after the etching after a 100% Cl_2 process[55]. When using a Si carrier

wafer, it can be inferred that the N-Si bonds that are formed (see Fig. 1) may even more slows down the Cl reaction with N, explaining why in this case the N/Ga ratio is the highest. This is also supported by the fact that the N-Si bond dissociation energy (437.1 ± 9.9 kJ/mol) is higher than that of Ga-N (205 kJ/mol)[45,56].

Increasing the ion energy increases both the sputtering effect and the activation of the chemical etching. Molecular dynamics simulations show a preferential sputtering of nitrogen atoms in a pure sputtering regime such as Ar^+, leading to a N-depleted surface because the etching yield of higher than Ga[57]. Increasing the bias could then lead to a decrease of the N/Ga ratio by enhancing the N sputtering. However, it is not necessary the observed trend, meaning that the increase of the ion energy in a Cl_2 plasma seems to contribute to the enhancement of the chemical etching of Ga.

For the photoresist carrier wafer, the N/Ga ratio remains very close to the one of the reference for any bias. We have no explanation for why the N/Ga ratio is the less impacted with the photoresist carrier wafer.

The case of SiO_2 carrier wafer is the only one showing for some bias voltage a reverse trend, namely a N/Ga ratio inferior to the reference one, conveying a N-depletion rather than Ga. Although the N/Ga ratio evolution with bias does not seem to be correlated with the amount of O present on the GaN surface, we think that the presence of O at the surface may play a role in the low N/Ga ratio in two ways. The XPS data reveal the formation of Ga-O bonds (especially at – 50 V) that may block some Ga attack sites by chlorine atom. And in parallel, it cannot be excluded that oxygen reacts with N to form NO volatile etch byproducts. Both phenomena lead to a decrease of the N/Ga ratio.

D. GaN surface roughness after etching

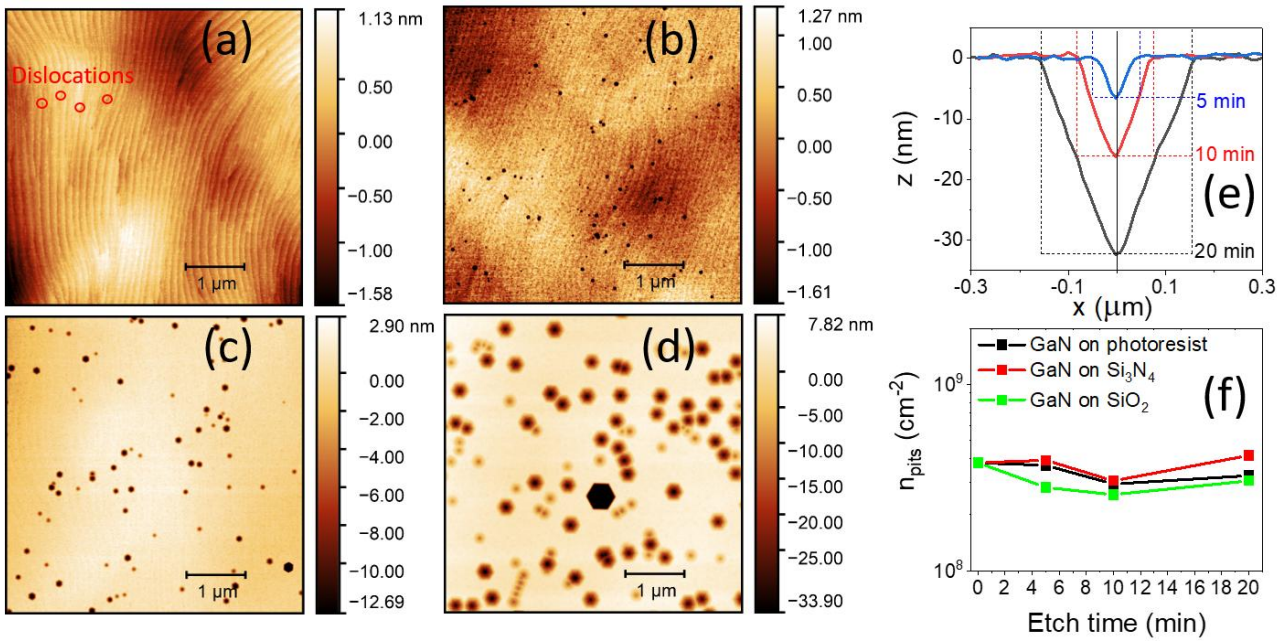

Fig. 11. AFM image of GaN surface before (a) and after etching in Cl_2 plasma with no bias and Si_3N_4 CW during (b) 5 min (c) 10 min (d) 20 min; (e) etch pit shape evolution with process time (f) etch pits density evolution with process time.

Figure 11 shows the GaN surface roughness evolution with time when exposed to Cl_2 plasma with unbiased carrier wafers. The case of GaN sample on a Si_3N_4 carrier wafer is shown, but exactly similar trend is observed with the photoresist and SiO_2 substrates. The case of Si wafer is different and will not be discussed here because XPS analyses reveal the formation of a $SiCl_x$ deposition on the GaN surface that prevents from drawing conclusions on the GaN surface roughness evolution.

The AFM image of the as-grown GaN surface (Fig 11a) shows the atomic steps, characteristic of the epitaxial growth and also reveals some few point defects positioned at surface step terminations.

These defects are known to correspond to the surface termination of pure-screw or mixed dislocations[58]. The etch pit density estimated for the as-grown sample is of 3.10^8 cm^{-2} which is close to the threading dislocation density of 4.10^8 given by the supplier and the RMS roughness is 0.3 ± 0.05 nm. By exposing the GaN surface to an unbiased Cl_2 plasma, hexagonal pyramid-shaped pits located at atomic step termination are formed on the GaN surface. These etch pits grow in diameter and depth with increasing processing time (Fig. 11b/c/d/e) but their density remain constant and similar to the as-grown sample (Fig. 11f). This leads to an increase of the RMS roughness with plasma exposure time. The fact that the location of the pits and their density are similar to the ones of the as-grown sample reveals that the defective region of the GaN sample is preferentially etched away under unbiased Cl_2 plasma.

Moreover, the hexagonal shape of the pits reflects crystallographic symmetry of the GaN lattice, suggesting a crystal orientation dependent etching. Similar defects have already been reported in the literature dealing with the wet etching of GaN. Lai *et al.* describes the formation mechanism of hexagonal holes when using a heated KOH solution on the GaN surface[59]. They correlate the degree of difficulty to etch a given crystallographic plane with the planar density and the number of dangling bonds on N atoms.

Based on this, they show that in a pure chemical type of etch the c plane is the harder to be etched while the r-plane is preferentially etched and turns into the (1011) plane with longer etching time, forming a hexagonal hole on the GaN surface.

Similar mechanisms may be involved in the unbiased Cl_2 plasma conditions used in this study. In these conditions the chemical aspect of the plasma is enhanced compared

to the physical one since ion energy is about the plasma potential of about 15-20 eV. The etching is mainly driven by the atomic chlorine present in the plasma. As the etch rate of the carrier wafer is extremely low (see Fig 5a), the atomic chlorine is fully available for the GaN etching. The atomic Cl preferentially etch the less dense r-plane compared to the c-plane, leading the hexagonal shaped defects. It is besides known that GaN c-plane (0001) is hardly etched with no or low energetic ions.

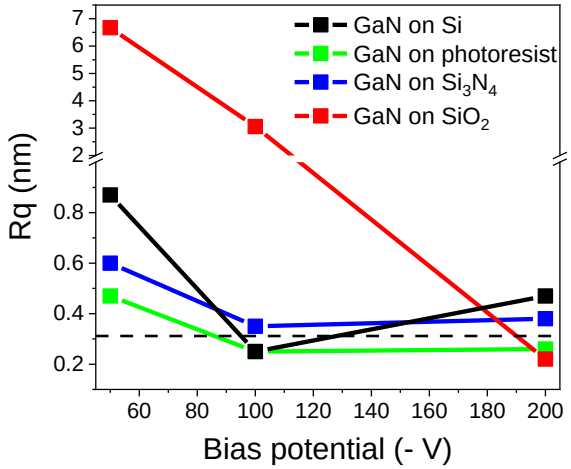

Fig. 12. GaN surface roughness as function of the carrier wafer and the bias potential during Cl_2 etching. *The dashed line represents the RMS reference value for the pristine GaN surface.*

AFM measurements are also performed after GaN etching in Cl_2 with different bias voltages and the Si, phororesist, SiO_2 and Si_3N_4 carrier wafers (Fig. 12).

The surface roughness of GaN after etching in Cl_2 is not much impacted if Si, photoresist or Si_3N_4 carrier wafers are used, except at low bias potential of − 50 V. At higher bias, the surface roughness values are quite similar to the ones of the pristine GaN (Fig. 11a), suggesting that the contaminants found on the GaN surface by XPS according to the wafer used play here a minor role in the roughness formation.

Regarding the SiO_2 substrate, the roughness is significantly higher than for the other substrates but is decreased down to similar low values at higher bias potential. We explain the significant surface roughness formation by the presence of the SiO_x residues at the surface (see Fig. 8 and Fig. 9) that act as micromask[17-19] and generate columnar defect. This is comforted by the fact that at higher bias, no Si is detected by XPS at − 200 V on the GaN surface and in parallel, the GaN surface roughness is smooth. The presence of GaO bonds may also have an impact in the roughness formation at low bias.

The evolution of the roughness with bias voltage is similar for all substrates. At low bias, the photoresist and Si carrier wafers present etch pits with an average depth about 2 nm (Fig. 13a/b), while the average depth is about 5-6 nm for Si_3N_4 (Fig. 13c) and 10 nm for the SiO_2 carrier wafer (Fig. 13d). As explained above, those etch pits are due to the presence of threading dislocations that are revealed by the preferential crystalline orientation etching driven by the chemical action of atomic chlorine. Thus, the etch pit depth logically correlates with the available atomic chlorine in the plasma which is a priori higher in the case of SiO_2 and Si_3N_4 that are etched less rapidly. For all substrates, the increase of the ion energy is beneficial for the preservation of the GaN surface roughness. At high bias potential, all GaN surfaces present a similar morphology as the pristine GaN (see Fig. 11a).

The roughness decrease with increasing bias can be explained by the activation of the surface-plane (c-plane) etching with the energetic ion bombardment, compared to the r-plane whose etching rate is not much impacted by the ion bombardment. This means that the preservation of the as-grown GaN surface roughness is a well-controlled balance between the ionic bombardment that drives the c- plane surface etching and the amount

of chlorine radicals that will be responsible for the r-plane etching and the enlargement of the initial surface defects. It should be noted that although the RMS roughness values at high bias is similar to the one of the pristine materials, the surface morphology is not exactly the same. The atomic steps are still visible at high bias but the AFM image is more blurred conveying an amorphisation of the GaN surface which may be detrimental for the electrical performance of the device. Finally, except in the presence of SiO_x etch byproducts, we have not seen an impact of the other contaminants (SiCl, C, H, F..) on the roughness.

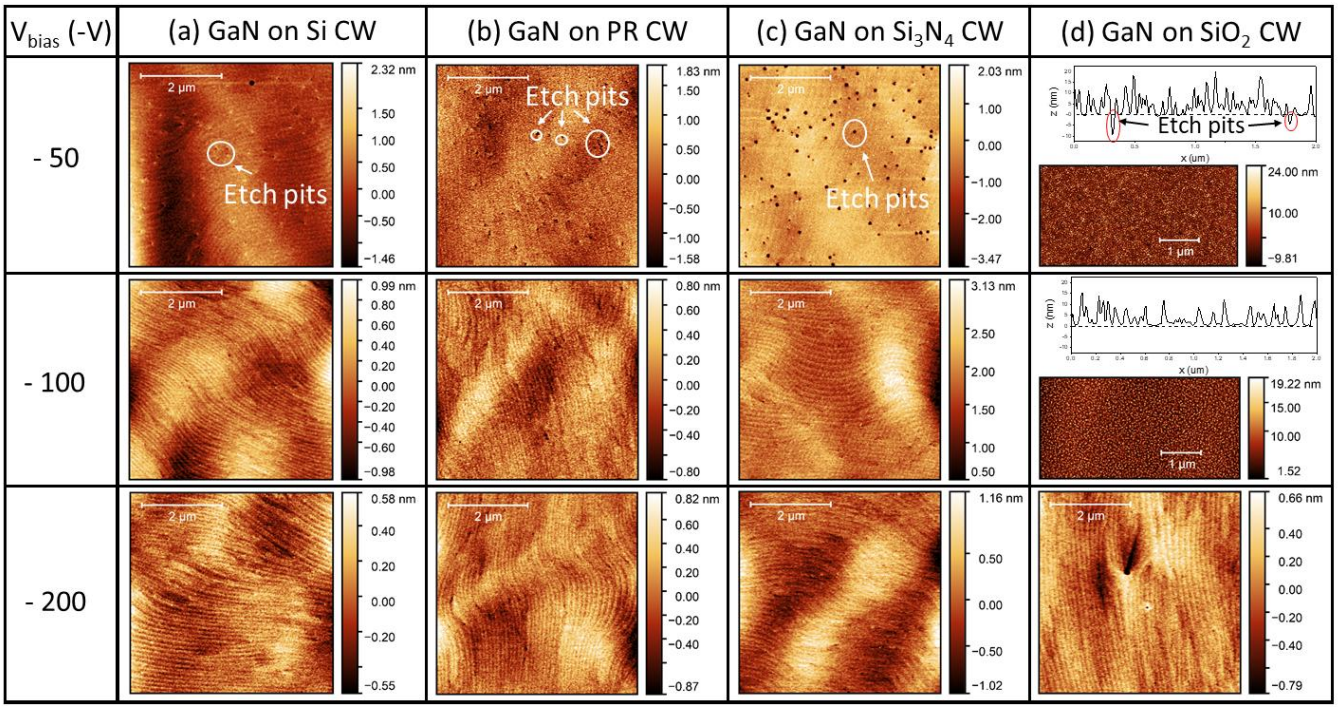

Fig. 13. AFM image of GaN surface after etching up to 100 nm in Cl_2 plasma as a function of bias voltage and carrier wafers a) Si, b) Photoresist, c) Si_3N_4, d) SiO_2.

IV. CONCLUSION

In this study, the influence of the carrier wafer during the GaN etching was investigated under various bias voltage and according to the carrier wafer used (Si, SiO_2, Si_3N_4, photoresist).

Firstly, a fitting protocol is proposed for the N 1s/Ga $L_2M_{4,5}M_{4,5}$ region in order to evaluate the N/Ga ratio when only a Al Kα X-ray source is available. The GaN etching characteristics are very sensitive to the physico-chemical properties of the plasma such as the atomic chlorine concentration or the ionic flux. The latter attributes are strongly influenced by the nature of the carrier wafer.

The higher etch rates of Si and the photoresist carrier wafers lead to a significant chlorine consumption compared to SiO_2 and Si_3N_4, which in turn lead to lower GaN etch rates and cause a major difference of the GaN:wafer selectivities.

Moreover, the carrier wafer etching leads to the ejection in the plasma of etch byproducts whose chemical nature will depend on the substrate being etched. OES data indicates that $SiCl_x$ products are predominant in the case of Si carrier wafer, CCl_x for photoresist wafer, while Si, SiCl, N_2 are detected for Si_3N_4 carrier wafer. In the SiO_2 case, OES data did not permit to evidence any etch byproduct. We suspect that the main product must be SiO, however the SiO vibrational bands overlap with the Cl_2 vibrational bands in the 200-300 nm range.

Consequently, the GaN surface contamination after etching is different according to the wafer used: a $SiCl_x$ reactive layer is formed on the GaN surface for Si carrier wafer, carbon is detected for photoresist substrate, and SiO_x in the SiO_2 case. Regarding Si_3N_4, no contamination coming from the substrate is identified, although it is difficult to assert

with certainty that the N detected on the GaN surface does not come from the Si_3N_4 wafer. Besides, in all cases, a thin GaCl reactive layer, less than 1 nm, is formed on the GaN surface, with the Si_3N_4 carrier wafer leading to the thinner reactive layer on the GaN surface. The N/Ga ratio in the Si, photoresist and Si_3N_4 carrier wafer cases shows that the exposition to a Cl_2 plasma generates a Ga-depleted surface, due to the more important reactivity of Cl with Ga rather than N, while with a SiO_2 carrier wafer, the interaction between O and the GaN surface induces Ga-O bonds that limits the Ga removal.

Surface roughness analysis demonstrates that the contaminants (Si, C, H) plays little role in the roughness formation. With a SiO_2 carrier wafer, the presence of both Si and O leads to a SiO_x reactive layer on the GaN surface which is responsible of a micromasking effect for low-bias processes.

At low bias, the etching by reactive radicals dominate and the Cl radicals preferentially etch the less dense r-plane compared to the c-plane. This leads to the formation of hexagonal shaped defects that are associated to screw-type threading dislocations. The fact that their density is similar to that of the pristine sample reveals that the defective region of the GaN sample is preferentially etched away under unbiased Cl_2 plasma. By increasing the ion energy, the etching of the c-plane is enhanced compared to the r-plane limiting the enlargement of the defects and thus limiting the surface roughness degradation. At high bias, similar surface roughness values as the pristine material is obtained but the quality of the AFM image suggests that the GaN surface is amorphized. This means that the preservation of the as-grown GaN surface roughness is a well-controlled balance between the ionic bombardment that drives the c-plane surface etching

and the amount of chlorine radicals that will be responsible for the r-plane etching and the enlargement of the initial surface defects.

The roughness decrease with increasing bias can be explained by the activation of the surface-plane etching with the energetic ion bombardment, compared to the r-plane whose etching rate is not much impacted by the ion bombardment. This means that the preservation of the as-grown GaN surface roughness is a well-controlled balance between the ionic bombardment that drives the c-plane surface etching and the amount of chlorine radicals that will be responsible for the r-plane etching and the enlargement of the initial surface defects.

Electrical characterizations are ongoing to evaluate the critical impact of roughness and contamination on the electrical behavior of the GaN.

ACKNOWLEDGMENTS

This research was supported by the French RENATECH network and the Nano 2022 program.

DATA AVAILABILITY

The data that support the findings of this study are available from the corresponding author upon reasonable request.

REFERENCES

[1]F. Roccaforte, G. Greco, P. Fiorenza, F. Iucolano, Materials **12**, 1599 (2019).

[2]X. A. Cao, A. P. Zhang, G. T. Dang, F. Ren, S. J. Pearton, J. M. van Hove, R. A. Hickman, R. J. Shul, L. Zhang, J. Electron. Mater **29**, 256-261 (2000).

[3]R. J. Shul, L. Zhang, A. G. Baca, C. G. Willison, J. Han, S. J. Pearton, F. Ren, J. Vac. Sci. Technol. A **18**, 1139–1143 (2000).

[4]Z. Liu, J. Pan, A. Asano, K. Ishikawa, K. Takeda, H. Kondo, O. Oda, M. Sekine, M. Hori, Jpn. J. Appl. Phys **56**, 026502 (2017).

[5]C. Romanitan, I. Mihalache, O. Tutunaru, C. Pachiu, J. Alloys Compd. **858**, 157723 (2021).

[6]Y.-Y. Wong, E. Y. Chang, T.-H. Yang, J.-R. Chang, J.-T. Ku, M. K. Hudait, W.-C. Chou, M. Chen, K.-L. Lin, J. Electrochem. Soc. **157**, H746-H749 (2010).

[7]S. Besend**ö**rfer, E. Meissner, F. Medjdoub, J. Derluyn, J. Friedrich, T. Erlbacher, Sci. Rep. **10**, 17252 (2020).

[8]S. Besend**ö**rfer, E. Meissner, T. Zweipfennig, H. Yacoub, D. Fahle, H. Behmenburg, H. Kalisch, A. Vescan, J. Friedrich, T. Erlbacher, AIP Adv. **10**, 045028 (2020).

[9]J. Kotani, J. Yaita, A. Yamada, N. Nakamura, K. Watanabe, J. Appl. Phys. **127**, 234501 (2020).

[10]R. J. Shul, G. B. McClellan, S. A. Casalnuovo, D. J. Rieger, S. J. Pearton, C. Constantine, C. Barratt, R. F. Karlicek, C. Tran, M. Schurman, Appl. Phys. Lett. **69**, 1119–1121 (1996).

[11]H.-S. Kim, G.-Y. Yeom, J.-W. Lee, T.-I. Kim, Thin Solid Films **341**, 180–183 (1999).

[12]J.-M. Lee, K.-M. Chang, I.-H. Lee, S.-J. Park, J. Electrochem. Soc. **147**, 1859 (2000).

[13]S. Zhou, B. Cao, S. Liu, Appl. Surf. Sci. **257**, 905–910 (2010).

[14]M. Tahhan, J. Nedy, S. H. Chan, C. Lund, H. Li, G. Gupta, S. Keller, U. Mishra, J. Vac. Sci. Technol. A **34**, 031303 (2016).

[15]N. Okada, K. Nojima, N. Ishibashi, K. Nagatoshi, N. Itagaki, R. Inomoto, S. Motoyama, T. Kobayashi, K. Tadatomo, AIP Adv. **7**, 065111 (2017).

[16]Y. Sun, X. Kang, Y. Zheng, K. Wei, P. Li, W. Wang, X. Liu, G. Zhang, Nanomaterials **10**, 657 (2020).

[17]E. Zhirnov, S. Stepanov, W. N. Wang, Y. G. Shreter, D. V. Takhin, N. I. Bochkareva, J. Vac. Sci. Technol. A **22**, 2336–2341 (2004).

[18]J. Ladroue, A. Meritan, M. Boufnichel, P. Lefaucheux, P. Ranson, R. Dussart, J. Vac. Sci. Technol. A **28**, 1226–1233 (2010).

[19]T. Urushido, H. Yoshida, H. Miyake, K. Hiramatsu, Jpn. J. Appl. Phys. **41**, L31 (2002).

[20]M. Bizouerne, E. Pargon, C. Petit-Etienne, S. Labau, S. David, M. Martin, P. Burtin, J. Vac. Sci. Technol. A **36**, 061305 (2018).

[21]https://www.techspray.com/silicone-free-heat-sink-compound

[22]F. González-Posada, J. A. Bardwell, S. Moisa, S. Haffouz, H. Tang, A. F. Braña, E. Muñoz, App. Surf. Sci. **253**, 6185–6190 (2007).

[23]J. E. Castle, D. Epler, J. S. Anderson, Proc. R. Soc. A **339**, 49–72 (1974).

[24]G. Schön, J. Electron Spectrosc. Relat. Phenom. **2**, 75–86 (1973).

[25]E. Antonides, E. C. Janse, G. A. Sawatzky, Phys. Rev. B **15**, 1669–1679 (1977).

[26]F. P. Larkins, J. Phys. C: Solid State Phys. **11**, 1965–1971 (1978).

[27]C. Lund, S. Thurgate, A. B. Wedding, Physical Review B **55**, 5455 (1997).

[28]J. Hedman, N. Maartensson, Phys. Scr. **22**, 176–178 (1980).

[29]R. Carin, J. P. Deville, J.Werckmann, Surf. Interface Anal. **16**, 65–69 (1990).

[30]S. D. Wolter, J. M. DeLucca, S. E. Mohney, R. S. Kern, C. P. Kuo, Thin Solid Films **371**, 153–160 (2000).

[31]M. Grodzicki, P. Mazur, A. Krupski, A. Ciszewski, Vacuum **153**, 12–16 (2018).

[32]Y. Zhao, H. Gao, R. Huang, Z. Huang, F. Li, J. Feng, Q. Sun, A. Dingsun, H. Yang, Sci. Rep. **9**, 16969 (2019).

[33]J. M. C. Thornton, P. Weightman, D. A. Woolf, C. J. Dunscombe, Phys. Rev. B **51**, 14459–14469 (1995).

[34]J. L. Bourque, M. C. Biesinger, K. M. Baines, Dalton Trans. **45**, 7678–7696 (2016).

[35]K. Sawangsri, P. Das, S. N. Supardan, I. Z. Mitrovic, S. Hall, R. Mahapatra, A. K. Chakraborty, R. Treharne, J. Gibbon, V. R. Dhanak, K. Durose, P. R. Chalker, Microelectron. Eng. **178**, 178–181 (2017).

[36]S. Béchu, A. Loubat, M. Bouttemy, J. Vigneron, J.-L. Gentner, A. Etcheberry, Thin Solid Films **669**, 425–429 (2019).

[37]D. Li, M. Sumiya, S. Fuke, D. Yang, D. Que, Y. Suzuki, Y. Fukuda, J. App. Phys. **90**, 4219–4223 (2001).

[38]R. A. Beach, E. C. Piquette, T. C. McGill, T. J.Watson, MRS Internet J. Nitride Semicond. Res. **4S1**, G6.26 (1999).

[39]C. J. Powell, A. Jablonski, NIST Electron Inelastic-Mean-Free-Path Database - Version 1.2, National Institute of Standards and Technology, Gaithersburg, MD, 2010.

[40]D. R. Lide, H. V. Kehiaian, CRC Handbook of Thermophysical and Thermochemical Data, CRC Press, 1994.

[41]K. Seshan, Handbook of Thin Film Deposition Techniques Principles, Methods, Equipment and Applications, Second Edition, CRC Press, 2002.

[42]F. T. Ferguson, J. A. Nuth, J. Chem. Eng. Data **53**, 2824–2832 (2008).

[43]TRCVP Vapor Pressure Database Version 2.2P, Thermodynamic Research Center, Texas A&M University, College Station, TX.

[44]B. Brunetti, V. Piacente, P. Scardala, J. Chem. Eng. Data **55**, 98–102 (2010).

[45]Y.-R. Luo, Comprehensive Handbook of Chemical Bond Energies, CRC Press, 2007.

[46]L.-B. Chang, S.-S. Liu, M.-J. Jeng, Jpn. J. Appl. Phys. **40**, 1242 (2001).

[47]H. Hahn, J. B. Gruis, N. Ketteniss, F. Urbain, H. Kalisch, A. Vescan, J. Vac. Sci. Technol. A **30**, 051302 (2012).

[48]K. Dogheche, B. Alshehri, G. Patriache, E. Dogheche, Photonics **8**, 68 (2021).

[49]R. Khare, A. Srivastava, V. Donnelly, J. Vac. Sci. Technol. A **30,** 051306 (2012).

[50]A Granier, M Vervloet, K Aumaille and C Vallee, Plasma Sources Sci. Technol. **12**, 89–96 (2003).

[51]M. Hasegawa, T. Tsutsumi, A. Tanide, S. Nakamura, H. Kondo, K. Ishikawa, M. Sekine, M. Hori, J. Vac. Sci. Technol. A **38,** 042602 (2020).

[52]C. Petit-Etienne, M. Darnon, P. Bodart, M. Fouchier, G. Cunge, E. Pargon, L. Vallier, O. Joubert, S. Banna, J. Vac. Sci. Technol. B **31,** 011201 (2013).

[53]P. Brichon, E. Despiau-Pujo, O. Mourey, O. Joubert, J. App. Phys. **118**, 053303 (2015).

[54]J. Ishikawa, H. Tsuji, M. Mimura, Y. Gotoh, in: Proceedings of 11th International Conference on Ion Implantation Technology, pp. 776–779.

[55]H.-S. Kim, G.-Y. Yeom, J.-W. Lee, T.-I. Kim, Thin Solid Films **341**, 180–183 (1999).

[56]D. Tzeli, A. A. Tsekouras, J. Chem. Phys. **128**, 144103 (2008).

[57]R. Kawakami, T. Inaoka, K. Tominaga, T. Mukai, Jpn. J. Appl. Phys. **48**, 08HF01 (2009).

[58]P. Visconti, K. M. Jones, M. A. Reshchikov, R. Cingolani, H. Morkoç, R. J. Molnar, Appl. Phys. Lett. **77**, 3532–3534 (2000).

[59]Y.-Y. Lai, S.-C. Hsu, H.-S. Chang, Y. S. Wu, C.-H. Chen, L.-Y. Chen, Y.-J. Cheng, Res. Chem. Intermed. **43**, 3563–3572 (2017).